



## Multiscale modeling algorithm for core images

Zhengji Li <sup>1,2</sup>, Xiaohai He <sup>1,\*</sup>, Qizhi Teng<sup>1,3</sup> and Honggang Chen<sup>1</sup>

<sup>1</sup>College of Electronics and Information Engineering, Sichuan University, Chengdu 610065, China

<sup>2</sup>College of Computer Science and Technology, Jincheng College of Sichuan University, Chengdu 610065, China

<sup>3</sup>Key Laboratory of Wireless Power Transmission of Ministry of Education, No. 24 South Section 1, 1<sup>st</sup> Ring Road, Chengdu, Sichuan, 610065, People's Republic of China



(Received 26 August 2019; revised manuscript received 19 January 2020; accepted 24 March 2020; published 8 May 2020)

Computed tomography (CT) images of large core samples acquired by imaging equipment are insufficiently clear and ineffectively describe the tiny pore structure; conversely, images of small core samples are insufficiently globally representative. To alleviate these challenges, the idea of a super-resolution reconstruction algorithm is combined with that of a three-dimensional core reconstruction algorithm, and a multiscale core CT image fusion reconstruction algorithm is proposed. To obtain sufficient image quality with high resolution, a large-scale core image is used to provide global feature information as well as information regarding the basic morphological structure of a large-scale pore and particle. Then the texture pattern and the tiny pore distribution information of a small-scale core image is used to refine the coarse large-scale core image. A blind image quality assessment is utilized to estimate the degradation model of core images at different scales. A multilevel pattern mapping dictionary containing local binary patterns is designed to speed up the pattern matching procedure, and an adaptive weighted reconstruction algorithm is designed to reduce the blockiness. With our method, images of the same core at different scales were successfully fused. The proposed algorithm is extensively tested on microstructures of different rock samples; all cases of the reconstructed results and those of the actual sample were found to be in good agreement with each other. The final reconstructed image contains both large-scale and small-scale information that can provide a better understanding of the core samples and inform the accurate calculation of parameters.

DOI: [10.1103/PhysRevE.101.053303](https://doi.org/10.1103/PhysRevE.101.053303)

### I. INTRODUCTION

Currently, gas and oil are the main energy resources; for this reason, a comprehensive three-dimensional (3D) reservoir model is needed to provide a better understanding of reservoirs. In particular, the pore-size distribution is one of the key characteristics of reservoirs [1–5].

Computed tomography (CT) is the primary imaging technique used to acquire 3D core images and the accuracy of a characteristic analysis is affected by image quality; however, its limitations lead to image quality being affected by the size of the sample. In large samples, the obtained large-scale images have better global representativeness and can better reflect the sample information on a macro scale, compared to smaller sample images, in which tiny pores are often missing. Furthermore, according to Adam *et al.* [6], the quality of a CT image is affected by scattered photons: the larger the size of the scanning sample, the more scattered the photons and the lower the quality of the acquired image. As shown in Fig. 1(a), the image resolution of the large sized image sample is insufficient and the image is particularly blurry; this negatively affects the accuracy of the calculation of the physical parameters, such as that of pore size distribution. Figure 1(a) shows one slice of a large size sample with a size

of  $\Phi = 25$  mm ( $14 \mu\text{m}/\text{pixel}$ ), wherein the pore/grain edge is blurred and the small pores are imperceptible.

Alternatively, when the sample image size is small, a high-quality small-scale image can be obtained, and some smaller pores that cannot be obtained with the large sample size can be clearly presented. Nonetheless, the macro representation of the high-quality small-scale images is insufficient. Figure 1(b) shows one slice of a small size sample, drawn from the same sample, with a size of  $\Phi = 2$  mm ( $0.875 \mu\text{m}/\text{pixel}$ ), whereas in Fig. 1(b) the details of the tiny pores are much clearer but the overall structure is not exhibited.

In addition, limited by the storage capacity, core images are compressed in some cases at the cost of quality. Lots of methods have been proposed to enhance the quality of the compressed images in recent years [7,8], and these works also apply to compressed core images.

In this paper we are focused on fusing a core image with various images of the same core sample at different scales. Doing so can allow the generation of a core image that provides information regarding both the overall structure and the tiny pore details.

A numerical construction method for multiscale pore networks was proposed by Jiang *et al.* [9]. The pore networks were constructed with the image sample at several different lengths and then represented in a single 3D model. In 2015, Gerke *et al.* [10] proposed a fusing method to integrate images at different scales into one single image using a predefined

\*Corresponding author: hxh@scu.edu.cn

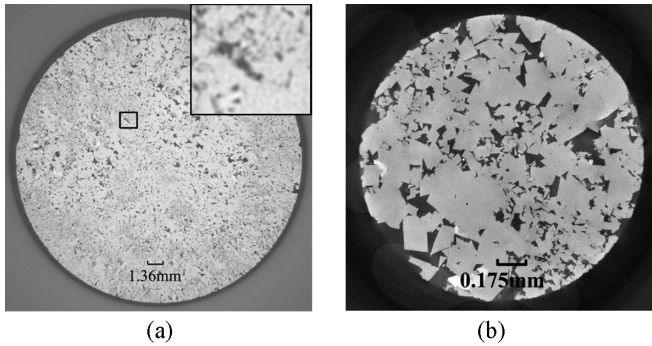


FIG. 1. Multiscale images of the same sample: (a) large-scale image at  $\Phi = 25$  mm ( $14 \mu\text{m}/\text{pixel}$ ) and (b) small-scale image at  $\Phi = 2$  mm,  $0.875 \mu\text{m}/\text{pixel}$ .

resolution. In their method, the samples with similar sizes and resolutions were created from rescaled correlation functions; the minerals and pores were then extracted and fused into one single binary image. In 2017, Tahmasebi [3] used 2D images of shale samples at different scales; the hybrid pattern- and pixel-based simulation method [11] was used to integrate those images into single images.

In 2018, Karsanina and Gerke [12] proposed a hierarchical annealing stochastic reconstruction method based on rescaled correlation functions; this method was shown to improve both the accuracy and computational efficiency of reconstructions with binary microstructures of different samples.

The results reconstructed by Gerke's method present a binary image, and the accuracy of image segmentation has a great influence on the reconstructed results; Jiang's reconstructed results are specified for the pore network. Tahmasebi's method is the first to reconstruct the image of shale samples at different scales in grayscale. However, theoretically, as per their methodical framework, degradation prediction of different scales images, which may cause distortion during the reconstruction procedure, was not utilized.

To obtain high-quality core sample images that show both the overall structure and tiny pore details, a method which fuses different scale images of the same core sample is proposed here. The large-scale core image is used to provide global feature information and the basic morphological structure, whereas the texture pattern, tiny pore shape, and distribution information of the small-scale core image are used to refine the large-scale core image. Overall, the development of the proposed method proceeds as follows: first, a degradation model predicting procedure is used to find the most probable degradation model; then, a pattern mapping dictionary with local binary patterns and a two-step searching algorithm are constructed; finally, a weighted reconstruction method is used to generate the fused image.

## II. METHODOLOGY

According to the super-resolution theory [13], the low-resolution model  $P_l$  is considered a blurred and downsampled version of the high-resolution structure  $P_h$ . The relation between them can be described as follows:

$$P_l = SBP_h + n, \quad (1)$$

where  $S$  is a down-sampled operator,  $B$  represents a blurring filter, and  $n$  is the additive noise.

By this theoretical understanding, the large-scale core image can also be seen as a degradation image of its small-scale core image. If it was possible to predict the degradation model between large-scale and small-scale images, this degradation model could be used to refine the large-scale image.

Usually, to predict the degradation model between multi-scale images, it is necessary to accurately register the images at different scales [14–16]. However, it is difficult to register the CT images of core samples, as shown in Fig. 1. Thus, here the random reconstruction theory is combined with the super-resolution theory.

First, the foundational idea of super-resolution technology, shown in Eq. (1), is used as a guide to generate the degradation model between large-scale and small-scale images.

Then, instead of accurately registering the images at different scales, the small-scale image is degraded with different methods; afterwards the degraded image that is most similar to the large-scale image is selected with the blind image quality assessment (BIQA) method. The selected degraded image and the small-scale image are then used to generate the pattern mapping dictionary. The pattern mapping dictionary stores pairs of degraded patterns and their corresponding original patterns and the degradation model can be represented with these paired patterns.

Subsequently, to refine the large-scale image, the resolution of the large-scale image is then adjusted according to the resolution of the small-scale image; the patterns are extracted from the adjusted large-scale image. Afterward, a simulation method similar to the random reconstruction method is used to refine the target image. The most similar degraded patterns and their corresponding original patterns are located in the pattern mapping dictionary; then these original patterns are used to refine the up-sampled large-scale patterns.

According to the theory mentioned above, several key issues must be addressed during the fusing process, including: (1) The degradation model prediction procedure; (2) the pattern mapping dictionary and the pattern searching algorithm; (3) the pattern similarity measurement; and (4) the fusing simulation method. In the following parts of this section, the solutions for these four key issues are explained in detail.

### A. Degradation model predicting procedure

The degradation model prediction procedure is one of the key challenges of the fusing modeling method. The basis of the modeling method is to establish the degradation model between multiscale images. As the large-scale image is considered to be a blurred and down-sampled version of the small-scale image, the parameters, such as frequency, gradient, brightness, and contrast, of the small-scale image are changed during the degradation procedure. These parameters can be used to evaluate the similarity between the degraded images and the large-scale image.

According to Mittal, natural scene statistics are excellent indicators of the degree of quality degradation of distorted images [17], such as the distribution of the locally normalized luminance [18], the gradient components and gradient magnitudes [19], locally mean subtracted and contrast normalized coefficients [17], the Log-Gabor filter responses [20], and the statistics of colors [21]. Zhang [19] pointed out that these distributions of natural images conform well to a Gaussian probability law; thus, a standard multivariate

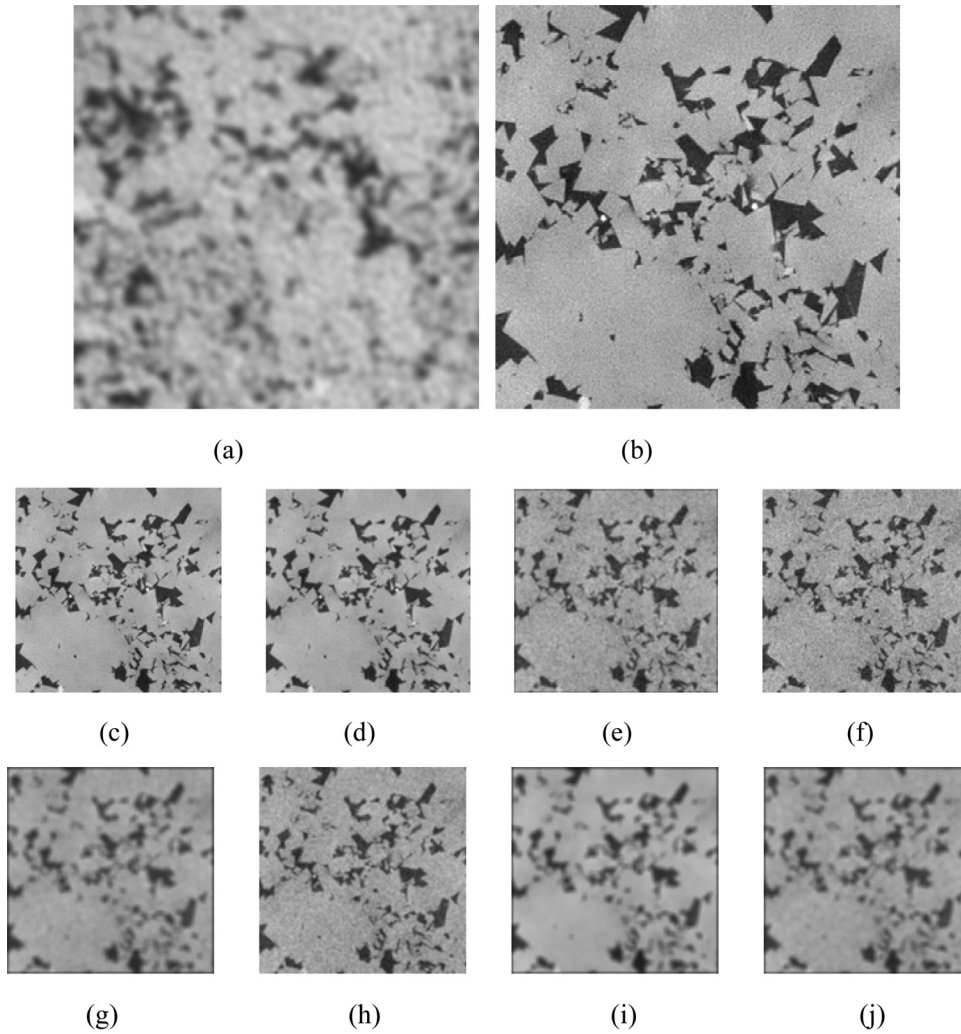


FIG. 2. Core sample and degradation images with different degradation model and parameters: (a) subimage of the large-scale image; (b) subimage of the small-scale image; (c) down-sampled image of (b); (d) degraded image no. 1: (c) with Gaussian filtering ( $\sigma = 1.6$ , kernel size =  $9 \times 9$ ); (e) degraded image no. 2: (c) with zero mean, Gaussian white noise with variance of 0.1 added followed by mean filtering (kernel size =  $9 \times 9$ ); (f) degraded image no. 3: (c) with zero mean, Gaussian white noise with variance of 0.1 added followed by Gaussian filtering ( $\sigma = 1.6$ , kernel size =  $9 \times 9$ ); (g) degraded image no. 4: (c) with zero mean, Gaussian white noise with variance of 0.1 added followed by mean filtering (kernel size =  $12 \times 12$ ); (h) degraded image no. 5: (c) with zero mean, Gaussian white noise with variance of 0.1 added followed by Gaussian filtering ( $\sigma = 1.6$ , kernel size =  $12 \times 12$ ); (i) degraded image no. 6: (c) with mean filtering (kernel size =  $19 \times 19$ ); (j) degraded image no. 7: (c) with zero mean, Gaussian white noise with a variance of 0.1 added followed by mean filtering (kernel size =  $20 \times 20$ ).

Gaussian (MVG) model was trained from a corpus of pristine naturalistic images, the quality of a test image was then predicted based on the distance between its MVG model and the standard MVG model. Zhang *et al.* [19] mentioned that quantitatively evaluating an image's perceptual quality has been among the most challenging problems of modern image processing and computational vision research. In 2015, they proposed a BIQA method [19]. With this method, by integrating the features of natural image statistics derived from multiple cues, five types of NSS features can be extracted from a collection of pristine naturalistic images. A multivariate Gaussian (MVG) mode, which is trained with these features, then serves as a reference model against which to predict the quality of the image patches. Using the trained multivariate Gaussian model, a Bhattacharyya-like distance is used to measure the quality of each test image patch. Then,

an overall quality score is obtained by average pooling, with the score indicating the image quality between the training image and the testing image. The lower the score, the greater the similarity of the qualities of the training images and the testing images.

To find the degradation model of core CT images at different scales, the BIQA method proposed by Zhang is adopted in our fusing framework. In our scenario, the BIQA score is used to estimate the qualities of large-scale images, and of degradation images of small-scale images, to ascertain the most suitable degradation image for constructing the degradation model between the large-scale image and the small-scale image. Thus, the degradation model can be used to constrain the multiscale modeling procedure.

As shown in Fig. 2, the small-scale image in Fig. 1 was down-sampled such that the actual size of each pixel is the

TABLE I. Image qualities calculated by Zhang's method.

Image	Quality
Subimage of the large-scale image	246.7
Subimage of the small-scale image	23.92
Down-sampled image of the small-scale image	50.5
Degraded image 1 [Fig. 2(d)]	109.0
Degraded image 2 [Fig. 2(e)]	169.2
Degraded image 3 [Fig. 2(f)]	116.1
Degraded image 4 [Fig. 2(g)]	237.0
Degraded image 5 [Fig. 2(h)]	173.8
Degraded image 6 [Fig. 2(i)]	226.1
Degraded image 7 [Fig. 2(j)]	243.7

same as that of the large-scale image in Fig. 1. Two subimages were then intercepted from each image. Subsequently, a series of degradation models were used on the high-resolution subimage to generate the degraded images. During the degradation procedure, the Gaussian filter and mean filter were used as the degenerate kernel filter, and the size of the filter was progressively increased from  $9 \times 9$  to  $20 \times 20$ . Furthermore, different types of noise were added.

At the beginning of the degradation model predicting procedure, 122 high-quality rock images were selected to train the standard MVG model. The distance between this and the MVG models of degraded images were calculated. This distance value was used to evaluate the quality of the degraded image.

The subimage of the large-scale image and the subimage and down-sampled images of the small-scale image are shown in Figs. 2(a)–2(c); several degraded images were randomly selected and included in Figs. 2(d)–2(j).

Figure 2 provides an overview of the core sample and their degradation images with different degradation models and parameters. Table I shows that the image qualities calculated with Zhang's method [19].

From Table I we can see that the BIQA value (243.7) of degraded image no. 7 [Fig. 2(j)] is closest to that (246.7) of the subimage of the large-scale image [Fig. 2(a)]. Meanwhile, visually, the quality of degraded image no. 7 [Fig. 2(j)] is particularly similar to that of the subimage of the large-scale image [Fig. 2(a)]. According to our theory, the degradation model generated from degraded image no. 7 [Fig. 2(j)] and the subimage of the small-scale image [Fig. 2(b)] can be used to further constrain the fusing procedure. Furthermore, as shown in Fig. 3, degraded image 7 [Fig. 2(j)] is selected and up-sampled to the same resolution of the small-scale image [Fig. 2(b)].

As demonstrated in Fig. 3, some of the clear, fine small pores in the small-scale image are indistinguishable in the up-sampled image of the selected degraded image. Those indistinguishable pores can cause errors in calculating pore size distribution. When the suitable degradation model is used to constrain the fusing procedure to generate the fused image, those indistinguishable pores in the large-scale image could be refined. This theory is experimentally tested in Sec. II B.

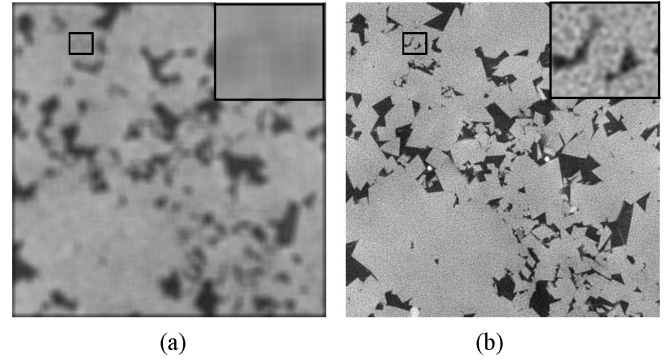


FIG. 3. Overview of up-sampled image and small-scale image: (a) Up-sampled image of the selected degraded image and (b) small-scale image.

### B. Structure of the pattern mapping dictionary and the pattern searching algorithm

As shown in Fig. 3, once the degraded image is selected, the pattern mapping dictionary can be constructed with the degraded image and the small-scale image. The down-sampling factor was assumed to be  $R$ , and the templates with a size of  $N \times N$  and  $M \times M$  ( $M = R \times N$ ) were used to collect the corresponding patterns from the degraded and small-scale images to create a pattern mapping dictionary.

The final fusing result and the computing time are greatly affected by the template size. The larger template size can describe larger area features, and the greater constraint conditions can be used during the fusing reconstruction, whereas the smaller template size can greatly speed up the simulation progress. Normally, in practice, the resolutions between the large-scale image and the small-scale image are quite different. Considering the reconstruction result and the process time, the template size was set to 17.

Research has shown that performance is enhanced when the rotation of the patterns is considered [22–24], pattern augmentation (rotation) was used to enrich the pattern mapping dictionary, with the rotation angles of  $0^\circ$ ,  $90^\circ$ ,  $180^\circ$ , and  $270^\circ$  considered, as shown in Fig. 4.

As the pattern matching process increases time costs, optimization of the pattern mapping dictionary and the search method is significant. To speed up the search method, the local binary pattern (LBP) was introduced. The LBP [25] was proposed in 1996 to measure texture; deriving rotation invariant versions of it is simple.

According to Ojala *et al.* [26], as shown in Fig. 5,  $T$  is defined as a pattern in a local  $3 \times 3$  neighborhood of a monochrome texture image, where  $g_i$  ( $i = 0, 1, 2, \dots, 8$ ) corresponds to the gray pixel values in the neighborhood.

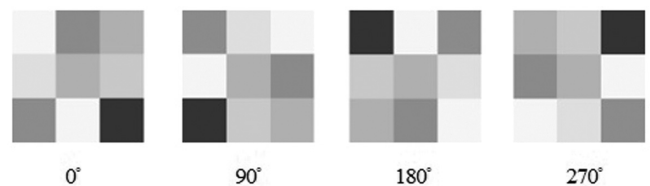


FIG. 4. Pattern augmentation.

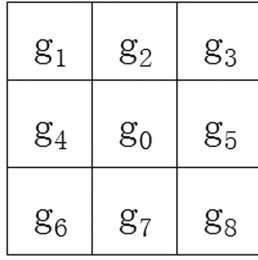


FIG. 5. T pattern and its pixel neighborhood.

The LBP is defined as

$$\text{LBP} = \sum_{i=1}^8 s(g_i - g_0)2^{i-1}, \quad (2)$$

where

$$s(x) = \begin{cases} 1, & x \geq 0, \\ 0, & x < 0. \end{cases} \quad (3)$$

As demonstrated in Fig. 6, the LBP of a pattern can be represented by eight binary digits. A simple shift operation can be used to derive the rotations of the LBP.

The pattern mapping dictionary contains three parts: (1) the small-scale patterns, (2) the degradation patterns, and (3) the LBP of the degradation patterns. The structure of the pattern mapping dictionary is illustrated in Fig. 7.

As the search method is also a key challenge, a two-step search method is thus proposed based on the pattern mapping dictionary. First, the LBP was used to perform a coarse search. In this step, the LBP of the large-scale pattern was retrieved from the large-scale image, several degradation patterns with the same LBP were found, and the rotations of the LBP were taken into consideration. To reduce the search time, only the main structure and the rotation angle were involved in this step.

Second, a similarity evaluation based on structural similarity (SSIM) was used to find the degradation pattern most similar to the large-scale pattern among the corresponding degradation patterns of the LBP patterns selected in the first step; the corresponding small-scale pattern of the most similar degradation pattern was then selected as the fusing pattern.

**C. Similarity measurement method of patterns**

Evaluation of pattern similarity is important in choosing the fusing pattern. According to Wang [27], the mean squared error is the most widely used of the full-reference quality metric methods; it is computed by averaging the squared intensity differences of distorted and reference image pixels. However, they are not very well matched in terms of visual

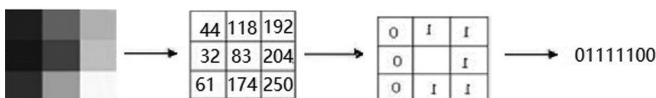


FIG. 6. Pattern and its LBP.

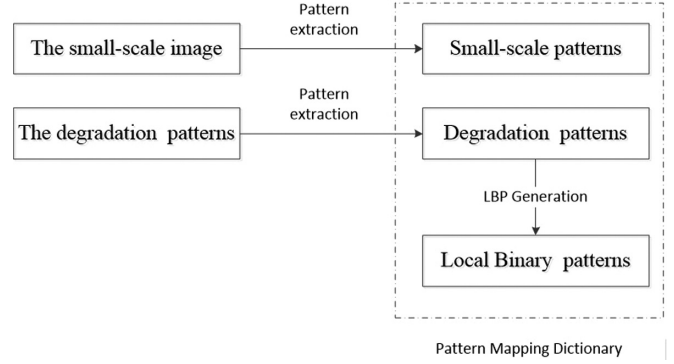


FIG. 7. Pattern mapping dictionary and its generation method.

quality, and a measure of SSIM is proposed. Figure 8 shows the system diagram of SSIM.

With the SSIM system, the task of similarity measurement is separated into three parts: luminance, contrast, and structure. The overall similarity measure of SSIM can be expressed as

$$\text{SSIM}(x, y) = [l(x, y)c(x, y)s(x, y)], \quad (4)$$

where  $l(x, y)$  is the luminance comparison function,  $c(x, y)$  is the contrast comparison function, and  $s(x, y)$  is the structure comparison function.

We define  $\mu_x, \mu_y$  as the mean value,  $\sigma_x, \sigma_y$  as the standard deviation, and  $\sigma_{xy}$  as the covariance of  $x$  and  $y$ , respectively. The SSIM can also be calculated with the following equation:

$$\text{SSIM}(x, y) = \frac{(2\mu_x\mu_y + C_1)(2\sigma_{xy} + C_2)}{(\mu_x^2 + \mu_y^2 + C_1)(\sigma_x^2 + \sigma_y^2 + C_2)}. \quad (5)$$

Normally we set  $C_1 = (K_1 \times L)^2$  and  $C_2 = (K_2 \times L)^2$ , where  $K_1 = 0.01, K_2 = 0.03$ , and  $L = 255$ . In our algorithm, the SSIM is used to evaluate the similarity between the large-scale pattern and the degradation pattern.

**D. Fusing simulation method**

The most similar pattern was selected according to the evaluation values, which were calculated by the similarity measurement method described in Sec. II C. The evaluation values refer to the degree of similarity between the large-scale pattern and the degradation pattern; the value is used as a weight in the fusing process. If the value is high, the small-scale pattern information can be used for

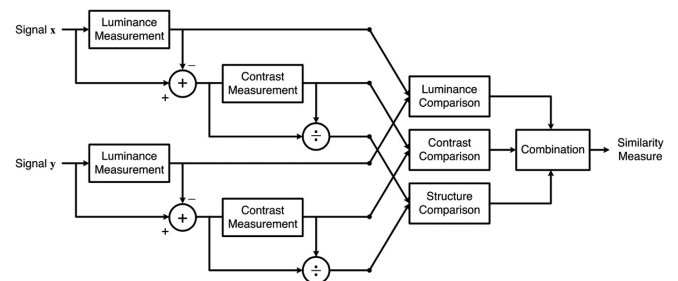


FIG. 8. Diagram of the SSIM system [27].

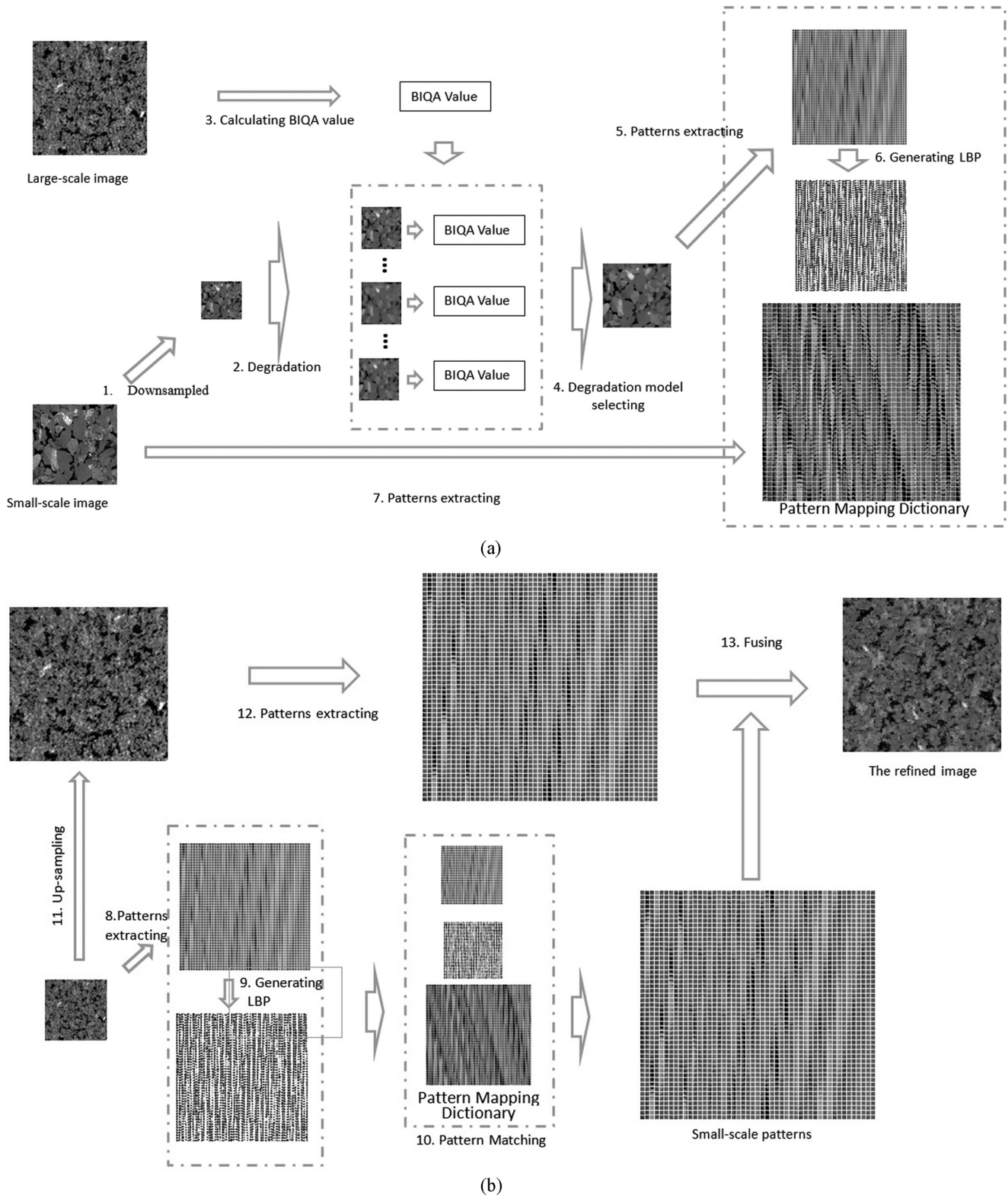


FIG. 9. Fusing procedure framework: (a) Pattern mapping dictionary generation and (b) simulation.

fusing; if not, the large-scale pattern information is used for fusing.

$L$  is the large-scale pattern with size  $p \times q$ , which is extracted from the large-scale image and requires refinement.  $L'$  (size  $p \times q$ ) and  $H'$  (size  $u \times v$ ) are the most similar cor-

responding degradation and small-scale patterns, respectively. Because the degradation pattern is the down-sampled version of small-scale pattern,  $u = p \times r$ ,  $v = q \times r$ , where  $r$  is the down-sampled factor. During the fusing procedure,  $L$  (size  $p \times q$ ) is up-sampled with an up-sampling factor  $r$  and  $L''$

(size  $u \times v$ ) is the up-sampling pattern. The refined pattern  $P$  (size  $u \times v$ ) is calculated as follows:

$$\begin{aligned} \omega_2 &= \text{SSIM}(L, L'), \\ \omega_1 &= 1 - \omega_2, \\ P &= L''\omega_1 + H'\omega_2, \end{aligned} \tag{6}$$

where  $\text{SSIM}(L, L')$  is the evaluation value of the similarity measurement between the patterns  $L$  and  $L'$ , the value of  $\text{SSIM}(L, L')$  is between 0 and 1, and  $\omega_1$  and  $\omega_2$  are the adaptive weight coefficients. The value of each point of  $P$  is computed with the values of corresponding locations of image  $L''$  and  $H'$  according to Eq. (6).

### E. Fusing procedure

To obtain a better understanding of the procedure, the entire workflow is divided into two parts: first, generation of the pattern mapping dictionary, and second, simulation.

The pattern mapping dictionary generation process includes the following steps:

(1) The small-scale image is down-sampled to the same resolution of the small-scale image with a down-sample factor  $r$ .

(2) A series of degradation models are used to generate the degraded image from the down-sampled small-scale image and the BIQA values of each degraded image are calculated.

(3) The BIQA value of the large-scale image is calculated.

(4) The most probable degraded image is selected according to the BIQA value.

(5) The degradation patterns are extracted from the most probable degraded image.

(6) The LBP is extracted from the degradation patterns.

(7) The small-scale patterns are extracted from the small-scale image.

(8) The degradation patterns, LBP, and small-scale patterns are used to construct the pattern mapping dictionary.

The simulation procedure consists of the following steps:

(9) The patterns are extracted from the large-scale image.

(10) The LBP are generated from the patterns extracted in step 8.

(11) The LBP and the patterns extracted in step 8 are used to find the most similar degradation patterns in the pattern mapping dictionary, and the corresponding small-scale patterns are located.

(12) The large-scale image is up-sampled with an up-sample factor  $r$ .

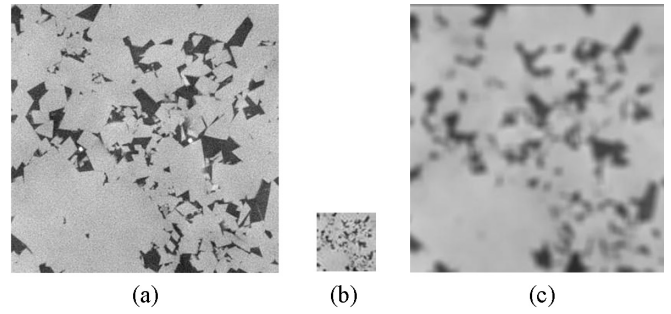
(13) The large-scale patterns are extracted from the up-sampled large-scale image.

(14) The small-scale patterns and the large-scale patterns are fused together according to Eq. (6) to generate the refined image.

The framework of the fusing procedure is shown in Fig. 9.

## III. RESULTS AND DISCUSSION

In this section the series of experiments performed to test our fusing reconstruction method are discussed. The aim of the first experiment was to test the effectiveness of the algorithm. Two small-scale images of the same rock sample were



Pore size distributions of the original image and the degraded image

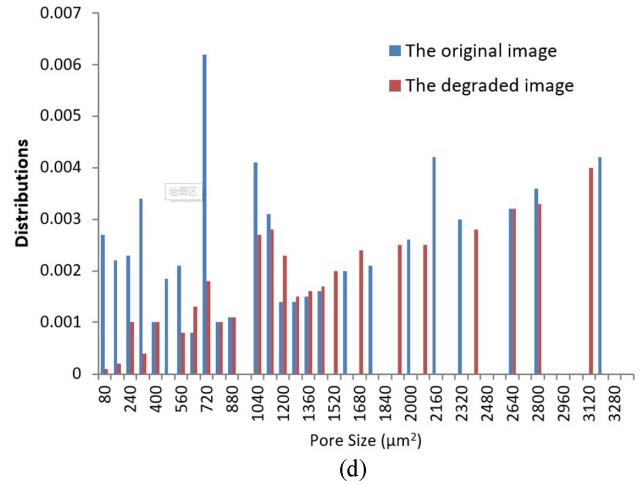


FIG. 10. Image of rock sample, down-sampled image, enlarged image, and pore size distributions: (a) original image of rock sample; (b) degraded image of (a) from a mean filter with a  $5 \times 5$  kernel size and a down-sample factor of 8; (c) enlarged image of the degraded image (b); and (d) pore size distributions of (a) and (b).

selected; one of them was down-sampled and degraded, and the resulting image was treated as the large-scale image, while the other was used to train the pattern mapping dictionary. Then, the pattern mapping dictionary was used to refine the generated large-scale image and generate the fused image. Finally, the fused image was compared to the original small-scale image.

As shown in Fig. 10, an image of a rock sample (a) was selected, and a mean filter with a  $5 \times 5$  kernel size was used on the down-sampled image of (a), with a down-sample factor of eight; (c) is the enlarged image of (b), and (d) is the pore size distributions of (a) and (b).

As shown in Fig. 10, the degraded image is blurred and some tiny pores are indistinguishable, although they are very clear in the original image. Additionally, the distributions of the tiny pores (with areas smaller than  $1000 \mu\text{m}^2$ ) in the original image are much wider than those in the degraded image; for pores whose areas are larger than  $1000 \mu\text{m}^2$ , the distributions change as the pore sizes change because of the degradation procedure, but the overall basic distribution is similar to the original image.

The other image of the same rock sample was selected as the small-scale image. As per the fusing procedure, the degradation model was first predicted; during this step, the

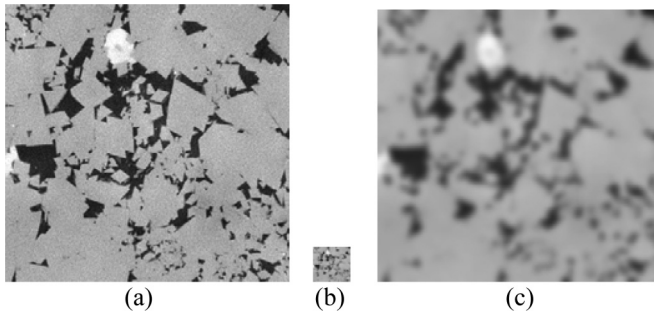


FIG. 11. (a) Small-scale image, (b) degraded image, and (c) enlarged image of (b).

small-scale image was down-sampled by a factor of 8. As the practically accurate degradation model was unknown and could be complex, during the degradation procedure, we attempted to use a simple degradation model to replace the actual degradation model. In this test, we designed a different degradation model to replace the real degradation model and validate our theory. A series of different degradation methods were used to generate degraded images. Then, the most probable degraded image was selected from the degraded images using the BIQA method introduced in Sec. II A.

As shown in Fig. 11, the most possible degraded image was generated with a Gaussian filter ( $\sigma = 1.6$ , kernel size:  $9 \times 9$ , BIQA value: 252.5), while the BIQA value of the large-scale image was 234.5 [Fig. 10(b)].

Subsequently, Figs. 11(a) and 11(b) were used to construct the pattern mapping dictionary, which was used to refine the

TABLE II. BIQA values of the original images, degraded image, and fused image.

	Original image	Degraded image	Fused image
BIQA value	25.8	234.5	38.0

large-scale image [Fig. 10(b)]. The fusing result and comparisons are shown in Fig. 12.

In Fig. 12, the fusing result (c) is generally much clearer than the enlarged image (b); as shown in the black boxes in (a), (c), and (d), the tiny pores in the original image are indistinguishable in the enlarged degraded image (c), while they can still be seen in (d). This indicates that our method can preserve these tiny pores in the fused image. Figures 12(e)–12(g) are the binary images of Figs. 12(a) (OSTU [28] method is used to segment the image), 12(c), and 12(d), respectively; visually, the binary image of the fusing result (g) is similar to the binary image of the original image (e).

Table II demonstrates the BIQA values of the original, degraded, and fused images shown in Fig. 12. The BIQA values indicate that the fused image is similar to the original image.

Figure 13 shows that the distributions of the tiny pores (with areas smaller than  $1000 \mu\text{m}^2$ ) in the original images are similar to those in the fused image; however, the distributions of the tiny pores in the original and fused images are much higher than those in the degraded image. For the pores with areas larger than  $1000 \mu\text{m}^2$ , the original, degraded, and fused images have similar distributions.

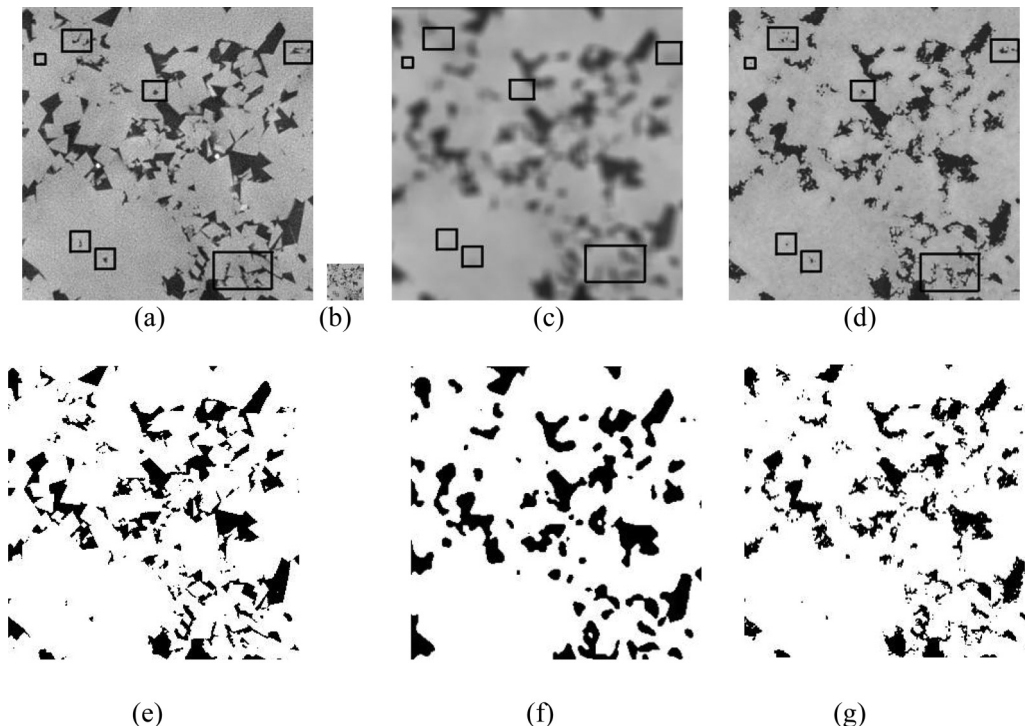


FIG. 12. Fusing results and comparisons: (a) original image, (b) degraded image, (c) enlarged image of (b), (d) fusing result, and (e)–(g) corresponding binary images.



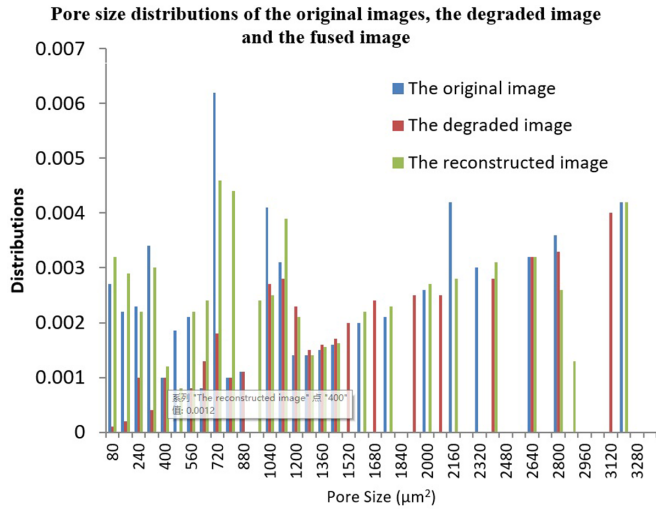


FIG. 13. Pore size distributions of the original images and the fused image.

This experiment demonstrates that not only can our method refine the large-scale image according to the small-scale image, but also the indistinguishable tiny pores in the large-scale image can be recovered. The previous test demonstrates the feasibility of our algorithm. Furthermore, to verify the stability and robustness of our method, the same core samples are used to repeat the same test ten times. As Fig. 14 shows, the pore size of the reconstruction results has similar distributions. Accordingly, the stability of our algorithm is verified.

In the next experiment, a large-scale image and small-scale image from the same rock sample were selected as the dataset. First, the large-scale image was taken as a slice of a 3D image of a large rock sample ( $\Phi = 25$  mm, the length of each pixel is  $5 \mu\text{m}$ , resolution:  $600 \times 600$ ) acquired using CT equipment. Then, a small part of the rock sample ( $\Phi = 5.7$  mm, length of each pixel:  $2.6 \mu\text{m}$ , resolution:  $300 \times 300$ ) was taken from the same sample, and a small-scale 3D image of it was obtained using the same CT equipment. Finally, a slice of the small-scale 3D image was selected as the small-scale image for testing. Figure 15 illustrates the large-scale and the small-scale images.

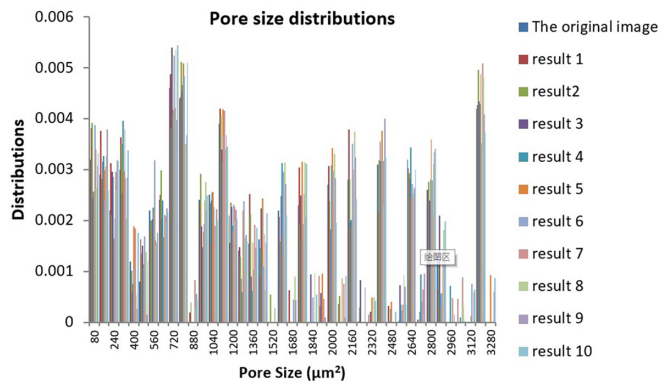


FIG. 14. Pore size distributions of ten reconstruction results with the same sample.

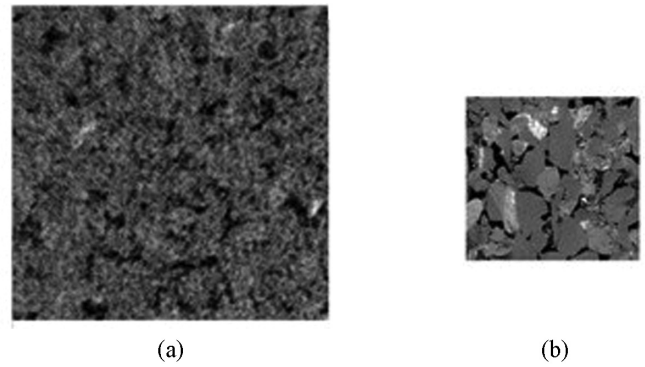


FIG. 15. Core samples for simulation: (a) large-scale image with  $\Phi = 25$  mm,  $5 \mu\text{m}/\text{pixel}$  and (b) small-scale image with  $\Phi = 5.7$  mm,  $2.6 \mu\text{m}/\text{pixel}$ .

The large-scale image shows a large region of the sample, but the image is blurred and the tiny pores are indiscernible. Alternatively, the small-scale image [Fig. 15(b)] covers a small region and presents the fine-scale feature and tiny pore information.

In the next experiment, the large-scale image [Fig. 15(a)] and the small-scale image [Fig. 15(b)] were used to reconstruct a fine-scale image including the fine-scale information.

The reconstructed result with a resolution of  $1200 \times 1200$  is shown in Fig. 16.

As shown in Fig. 16, the reconstructed result has a significant improvement in clarity; it retains the main structure of the large-scale image. Table III shows the BIQA values of the large-scale image, small-scale image, and reconstructed result. It is clear that the BIQA value of the reconstructed result is much closer to the small-scale image than that of

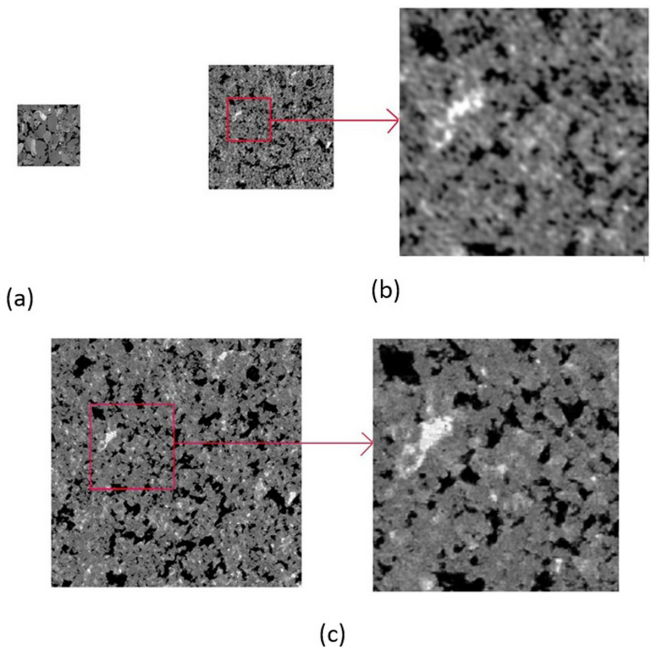


FIG. 16. Multiresolution images of rock sample and reconstructed results: (a) small-scale image, (b) large-scale image, and (c) reconstructed result.

TABLE III. BIQA values of the large-scale image, small-scale image, and reconstructed result.

	Large-scale image	Small-scale image	Reconstructed result
BIQA value	215.3	66.9	82.6

the large-scale image. Figure 17 demonstrates the binary images converted from the images in Fig. 16 with the same binarization method.

As shown in Figs. 16 and 17, the large pores in the two images have the similar locations and distributions, whereas the binary image of the reconstructed result can show many more tiny pore information than that of the large-scale image. For further comparison, the pore-size distributions are shown in Fig. 18.

As shown in Fig. 18, the distributions of the tiny pores (with areas smaller than  $2500 \mu\text{m}^2$ ) in the small-scale image are similar to those in the reconstructed image and much higher than those in the large-scale image. For the pores with areas larger than  $2500 \mu\text{m}^2$ , the distributions in the large-scale image and reconstructed image are similar to each other, and slightly higher than those in the small-scale image. The comparisons in Figs. 16–18 indicate that our method can refine the large-scale image, as the reconstructed image contains both large-scale and small-scale information. To verify the stability and robustness of our method, the same core samples were used to repeat the test ten times. The results of this are shown in Fig. 19, wherein it can be seen that the pore size of the reconstruction results have a similar distribution, thus verifying the stability of our algorithm.

To test the performance of the proposed pattern mapping dictionary and the searching algorithm, ten pairs of rock samples were used to test the pattern mapping dictionary and the searching algorithm. Each sample contains 4 000 000 simulating patterns and a pattern mapping dictionary with 360 000 pairs of atoms. This experiment is designed to test: (1) reconstruction time and (2) accuracy.

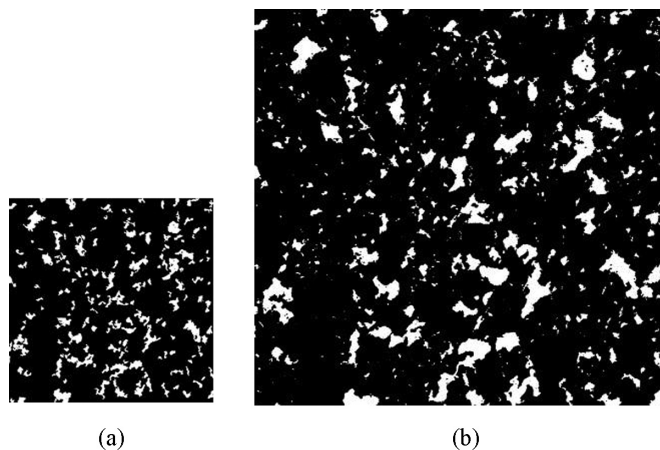


FIG. 17. Binary images of (a) the large-scale image and (b) the reconstructed result.

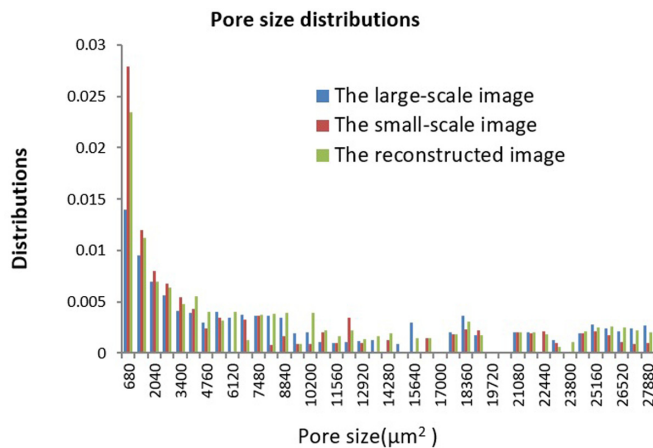


FIG. 18. Comparison of pore size distributions.

In the first step, the pattern mapping dictionary without LBP and the normal searching method are used, and the simulation time and the searching results are then recorded. These searching results are treated as the benchmark to test the searching accuracy for the next step.

In the second step, the proposed pattern mapping dictionary and the searching method are used. The reconstruction time is then recorded and the searching results compared with the benchmark generated in the first step. The simulation time and accuracy are shown in Table IV.

As shown in Table IV, the average reconstruction time is greatly reduced by using the proposed pattern mapping dictionary and searching method, whereas the proportion of the same searching results is very high.

The fusing method was also extended for 3D rock images, with the experiment for such described below. Figure 20 illustrates the large-scale and small-scale 3D images of the same rock sample in the previous experiment, as well as the reconstructed result and the visual comparison of slices. Therein, it can be seen that the reconstructed result not only has a significant improvement in clarity, but also retains the main structure of the large-scale image.

Table V shows the BIQA values of the large-scale image, small-scale image, and reconstructed result. As the BIQA

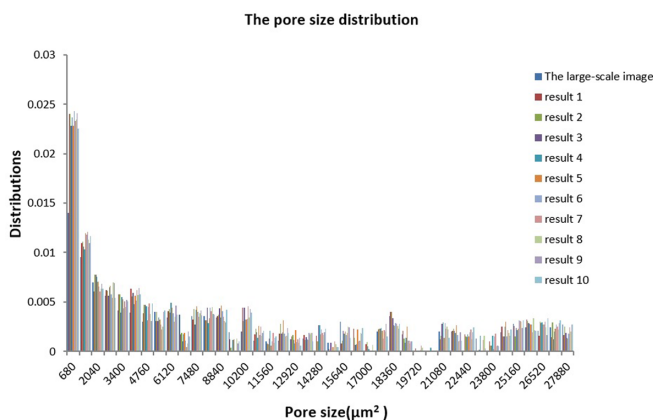


FIG. 19. Pore size distributions of ten reconstruction results with the same sample.

TABLE IV. Simulation time and accuracy comparisons.

Sample No.	Simulation time of first step (s)	Simulation time of second step (s)	Accuracy
1	54 385	30 756	95.99%
2	63 731	27 063	93.51%
3	63 085	28 517	98.07%
4	58 093	31 007	94.82%
5	56 363	34 072	93.85%
6	54 505	28 460	91.64%
7	55 181	31 686	92.39%
8	64 582	32 281	98.57%
9	54 912	30 662	91.35%
10	57 207	33 035	95.92%
Average	58 204	30 754	94.61%

method is for 2D images, the BIQA values of the 3D images are the averages of those of the 3D image slices. It is clear that the BIQA value of the reconstructed result is much closer to that of the small-scale image than that of the large-scale image.

As shown in Fig. 21, the distributions of the tiny pores (with volumes lower than  $5000 \mu\text{m}^3$ ) in the small-scale 3D image are similar to those in the reconstructed 3D image and much higher than those in the large-scale 3D image. For pores with volumes higher than  $2500 \mu\text{m}^3$ , the distributions in the three 3D images are similar.

The comparison in Fig. 21 indicates that not only can our method refine the large-scale image, but also that the reconstructed image contains both large-scale and small-scale information.

In addition to the visual comparison, quantitative analyses of our method, including the BIQA and pore-size distribution, are described herein. All the parameters show that our method can refine the large-scale image and restore the tiny pore information lost in the large-scale image.

IV. CONCLUSION

As the images of large core samples are not sufficiently clear and do not effectively describe the tiny pore structure, and images of small core samples are not sufficiently globally representative, a multiscale core image fusion method was proposed. The proposed method can be used to improve the image quality of large-scale core images and recover tiny pore information based on small-scale images.

In the proposed method, a BIQA algorithm was used to evaluate the image quality between the degraded image and the low-resolution image, and to predict the degradation

TABLE V. BIQA values of the large-scale image, small-scale image, and the reconstructed result.

	Large-scale image (average)	Small-scale image (average)	Reconstructed result (average)
BIQA value	238.2	62.8	92.7

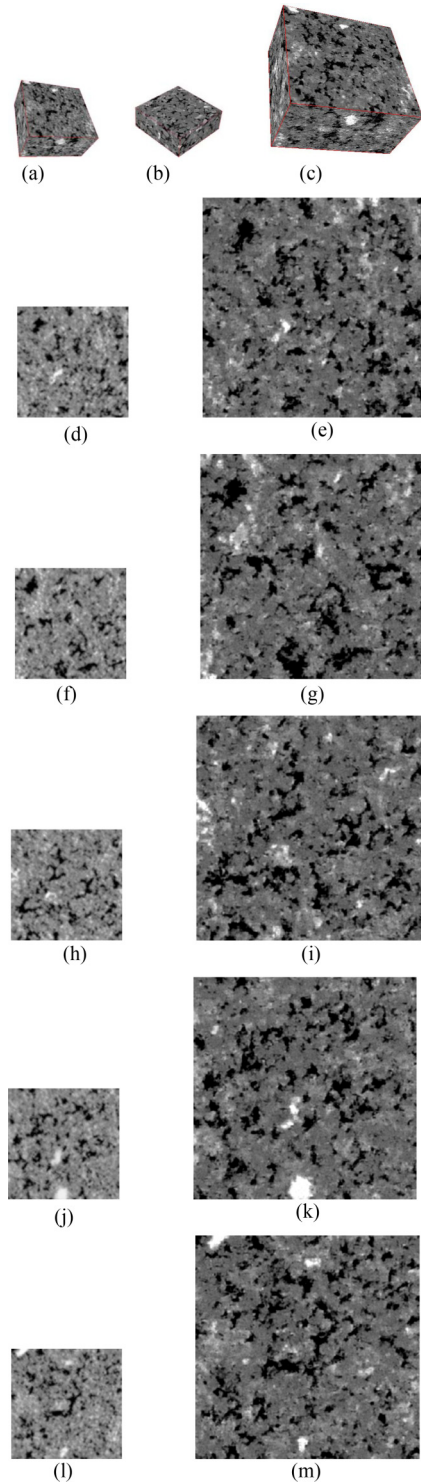


FIG. 20. Overview of rock sample and reconstructed results: (a) Large-scale 3D image; (b) small-scale 3D image enlarged twice; and (c) reconstructed result. Visual comparison of slices of the large-scale 3D image and reconstructed result: (d) tenth slice of the large-scale 3D image; (e) tenth slice of the reconstructed 3D image; (f) 50th slice of the large-scale 3D image; (g) 50th slice of the reconstructed 3D image; (h) 100th slice of the large-scale 3D image; (i) 100th slice of the reconstructed 3D image; (j) 150th slice of the large-scale 3D image; (k) 150th slice of the reconstructed 3D image; (l) 200th slice of the large-scale 3D image; and (m) 200th slice of the reconstructed 3D image.

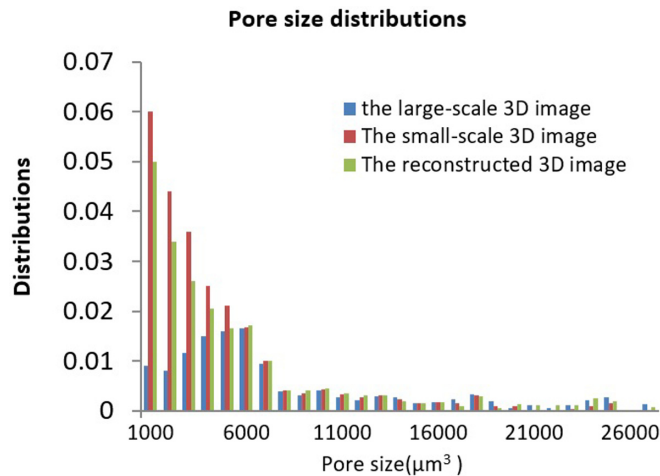


FIG. 21. Comparison of pore size distributions.

model. A pattern mapping dictionary with LBP and a corresponding two-step searching algorithm were designed to achieve improved pattern matching and augment reconstruction speeds, and an adaptive weighted reconstruction algorithm was proposed. Several evaluation experiments show that our method can fuse images of the same core at different scales; the fused image can maintain long-range and overall structural information of the large-scale image, as well as recover tiny pore distribution information from a small-scale image.

The fused images can provide a better understanding of core structures, as well as help in the accurate calculation of

physical parameters, such as porosity, pore size distribution, and permeability calculation.

The method proposed here can be further improved in future research. In the degradation model predicting procedure, as the degradation models are tested and selected manually, an autodegradation model predicting method is necessary for quick and improved predictions. Furthermore, although the LBP and two-step searching algorithm were used to increase the simulation speed, the fusing method still consumes a considerable amount of time; thus, a fusing method based on neural network should be considered in future studies.

#### ACKNOWLEDGMENTS

The proposed method in this paper is tested with our private sandstones datasets which were provided by the China National Petroleum Corporation. We would like to thank the editors and anonymous reviewers, whose comments and suggestions helped to improve the paper significantly. We would also like to thank Editage [29] for English language editing. This work was supported by the National Natural Science Foundations of China (Grants No. 61871279 and No. 61372174).

Z.L. fully participated in this project, including designing and coding, system implementation, experiments, and manuscript preparation. X.H. and H.C. made substantial contributions to the conception and development of the underlying ideas. Q.T. managed the project, and was accountable for all aspects of the work, including ensuring that the results were accurate.

- [1] A. Mehmani, M. Prodanovic, and F. Javadpour, Multiscale, multiphysics network modeling of shale matrix gas flows, *Transp. Porous Media* **99**, 377 (2013).
- [2] M. E. Naraghi and F. Javadpour, A stochastic permeability model for the shale-gas systems, *Int. J. Coal Geol.* **140**, 111 (2015).
- [3] P. Tahmasebi, Nanoscale and multiresolution models for shale samples, *Fuel* **217**, 218 (2018).
- [4] K. Liu, M. Ostadhassan, J. Zhou, T. Gentzis, and R. Rezaee, Nanoscale pore structure characterization of the Bakken shale in the USA, *Fuel* **209**, 567 (2017).
- [5] M. Liang, Z. Wang, L. Gao, C. Li, and H. Li, Evolution of pore structure in gas shale related to structural deformation, *Fuel* **197**, 310 (2017).
- [6] G. Adam, Y. S. Yoav, C. Yonatan, and G. Rajiv, X-ray computed tomography through scatter, *ECCV* **11218**, 37 (2018).
- [7] H. Chen, X. He, C. An *et al.*, Deep wide-activated residual network based joint blocking and color bleeding artifacts reduction for 4:2:0 JPEG-compressed images, *IEEE Signal Process Lett.* **26**, 79 (2019).
- [8] X. Zhang, W. Lin, R. Xiong, X. Liu, S. Ma, and W. Gao, Low-rank decomposition based restoration of compressed images via adaptive noise estimation, *IEEE Trans. Image Process* **25**, 4158 (2016).
- [9] Z. Jiang, M. I. J. van Dijke, K. S. Sorbie, and G. D. Couples, Representation of multiscale heterogeneity via multiscale pore networks, *Water Resour. Res.* **49**, 5437 (2013).
- [10] K. M. Gerke, M. V. Karsanina, and D. Mallants, Universal stochastic multiscale image fusion: An example application for shale rock, *Sci. Rep.* **5**, 15880 (2015).
- [11] P. Tahmasebi, HYPPS: A hybrid geostatistical modeling algorithm for subsurface modeling, *Water Resour. Res.* **53**, 5980 (2017).
- [12] M. V. Karsanina and K. M. Gerke, Hierarchical Optimization: Fast and Robust Multiscale Stochastic Reconstructions with Rescaled Correlation Functions, *Phys. Rev. Lett.* **121**, 265501 (2018).
- [13] W. R. Liu and S. T. Li, Multi-morphology image super-resolution via sparse representation, *Neurocomputing* **120**, 645 (2013).
- [14] P. Vandewalle, S. Sússtrunk, and M. Vetterli, A frequency domain approach to registration of aliased images with application to super-resolution, *EURASIP J. Adv. Signal Process.* **2006**, 071459 (2006).
- [15] P. Vandewalle, L. Sbaiz, S. Suesstrunk, and M. Vetterli, Registration of aliased images for super-resolution imaging, *Proc. SPIE* **6077**, 607702 (2006).

- [16] R. Y. Tsai and T. S. Huang, Multiframe image restoration and registration, *Advances in Computer Vision and Image Processing* **8**, 317 (1984).
- [17] A. Mittal, R. Soundararajan, and A. C. Bovik, Making a “completely blind” image quality analyzer, *IEEE Signal Process Lett.* **20**, 209 (2013).
- [18] D. L. Ruderman, The statistics of natural images, *Network-Comput. Neural Syst.* **5**, 517 (1994).
- [19] L. Zhang, L. Zhang, and A. C. Bovik, A feature-enriched completely blind image quality evaluator, *IEEE Trans. Image Process.* **24**, 2579 (2015).
- [20] D. J. Field, Relations between the statistics of natural images and the response properties of cortical-cells, *J. Opt. Soc. Am. A* **4**, 2379 (1987).
- [21] D. L. Ruderman, T. W. Cronin, and C. C. Chiao, Statistics of cone responses to natural images: Implications for visual coding, *Opt. Soc. Am. A* **15**, 2036 (1998).
- [22] J. Zhang, H. Zhao, and J. Liang, Continuous rotation invariant local descriptors for texton dictionary-based texture classification, *Comput. Vision Image Understanding* **117**, 56 (2013).
- [23] L. Lv, Z. Chen, Z. Zhang, T. H. Fan, and L. Z. Xu, Object tracking based on support vector dictionary learning, *Signal Image Video Process.* **12**, 1189 (2018).
- [24] T. Li, X. H. He, Q. Z. Teng, and X. Q. Wu, Rotation expanded dictionary-based single image super-resolution, *Neurocomputing* **216**, 1 (2016).
- [25] T. Ojala, M. Pietikainen, and D. Harwood, A comparative study of texture measures with classification based on feature distributions, *Pattern Recognit.* **29**, 51 (1996).
- [26] T. Ojala, M. Pietikäinen, and T. Mäenpää, Gray scale and rotation invariant texture classification with local binary patterns, in *Computer Vision - ECCV 2000, ECCV 2000*, Lecture Notes in Computer Science, Vol. 1842 (Springer, Berlin, Heidelberg, 2000), pp. 404–420.
- [27] Z. Wang, A. C. Bovik, H. R. Sheikh, and E. P. Simoncelli, Image quality assessment: From error visibility to structural similarity, *IEEE Trans. Image Process.* **13**, 600 (2004).
- [28] N. Ostu, A threshold selection method from gray-level histogram, *IEEE Trans. Syst., Man, and Cybernetics* **9**, 62 (1979).
- [29] [www.editage.cn](http://www.editage.cn).